

The L–H transition in tokamaks: power threshold, density minimum and toroidal-field asymmetry

B. De Lucca,* P. Ricci, B. Labit, D. Mancini, L. N. Stenger, and Z. Tecchioli
*École Polytechnique Fédérale de Lausanne (EPFL),
 Swiss Plasma Center (SPC), CH-1015 Lausanne, Switzerland*
 (Dated: May 6, 2026)

Flux-driven two-fluid simulations in a diverted tokamak exhibit a confinement transition when a critical heating threshold is exceeded, as in experimental observations of the L–H transition. The simulations show that electromagnetic drift-wave turbulence spontaneously generates a sheared $\mathbf{E} \times \mathbf{B}$ flow responsible for transport suppression in the edge. The toroidal-field asymmetry effect arises from time-reversal symmetry breaking by finite collisionality, as demonstrated by a quasilinear calculation of the turbulent momentum flux. First-principles scaling laws are derived for the L–H power threshold in the high- and low-density branches, for the density minimum, and for the minimum power, all matching or surpassing existing empirical scalings.

Above a threshold input power, turbulence in the edge region of fusion devices undergoes a rapid suppression, leading to a factor ~ 2 increase in the energy confinement time. Known as the L–H transition [1], this mechanism is considered essential to achieve burning plasma conditions in future devices, including ITER [2] and SPARC [3]. Despite numerous theoretical proposals [4–10], the physics underlying the L–H transition remains debated, as no existing model simultaneously accounts for several well-established experimental observations. These include the non-monotonic dependence of the threshold power, P_{LH} , on plasma density [11] and the observation that the threshold power is generally lower when the ion ∇B drift points from the core region toward the X -point in a diverted geometry (*favourable* configuration) [12, 13]. For densities above a critical value, called the density minimum, P_{LH} is well-described by the empirical scaling law [14]:

$$P_{\text{LH}}^{\text{ITPA}} = 0.0488 \bar{n}_{e20}^{0.717} B^{0.803} S^{0.941} \text{ [MW]}, \quad (1)$$

with \bar{n}_{e20} the line-averaged density in 10^{20} m^{-3} , B the magnetic field strength in T, and S the plasma surface area in m^2 . Though edge-transport bifurcations have been observed several times in global flux-driven turbulence simulations [15–17], their relevance to the experimental L–H transition observations remains unclear, and first-principles-based predictive capabilities are lacking.

Here, we present power-ramp simulations, starting from L–mode turbulence, carried out with the global flux-driven code GBS [18, 19], which solves the drift-reduced Braginskii equations. These simulations exhibit a confinement transition occurring at lower power in the favourable toroidal-field configuration, and based on these results, we derive a theory of the L–H transition with predictive capabilities.

The physical model solved by GBS is reported in detail in [19]. Using a fluid model is justified by the large edge collisionality in existing and future tokamaks. For typical L-mode parameters in TCV [20], the ratio of elec-

tron mean-free-path to connection length in the edge is small $\lambda_e/L_{\parallel} \lesssim 0.1$, with comparable values in AUG [5], and similar values expected in ITER and SPARC. The simulation parameters at the separatrix are $R/\rho_s = 500$, $\nu = 5 \times 10^{-2} c_s/R$, $a/R \simeq 0.3$, $m_i/m_e = 800$, $Z = 1$, and $\beta = 10^{-4}$, where R is the tokamak major radius, $\rho_s = c_s/\Omega_i$ is the sound Larmor radius, with $c_s = \sqrt{T_e/m_i}$ the ion sound speed and $\Omega_i = ZeB/m_i$ the cyclotron frequency, $\nu = e^2 n/(m_i \sigma_{\parallel})$ is the collisional frequency, a is the minor radius, m_i/m_e is the ion-to-electron mass ratio, Z is the ion charge number, and β is the electron plasma beta. The magnetic field $\mathbf{B} = \sigma_T R |B_{\varphi}| \nabla \varphi + \sigma_p \nabla \varphi \times \nabla \psi$ is that of a diverted lower-single-null tokamak, with edge safety factor $q_a \simeq 4$ and magnetic shear $\hat{s}_a \simeq 2$, and previously used in Ref. [16]. The plasma current direction is encoded in $\sigma_p \equiv \text{sign}(\mathbf{I}_p \cdot \nabla \varphi)$ and the favourable configuration corresponds to $\sigma_T \equiv \text{sign}(\mathbf{B} \cdot \nabla \varphi) = -1$.

Starting from L–mode simulations in quasi-steady-state, the input power is suddenly increased by a factor $\simeq 1.4$ at time $t = 0$. This is achieved by raising the heating sources in the core, while keeping the density source constant, with equal ion and electron heating. Figure 1 shows time traces of input power, P_{in} , energy confinement time, τ_E , and the radial electric field minimum, E_r^{min} . In the favourable configuration, $\sim 10R/c_s$ after additional heating is injected, a fast transport bifurcation occurs on a timescale of $\sim 5R/c_s$, with τ_E increasing by a factor ~ 2 . After an initial overshoot, the confinement time stabilises at a factor ~ 1.5 larger than its initial value. The flux-surface-averaged pressure and radial electric field profiles are shown in Fig. 2 as a function of distance from the separatrix, $r - r_{\text{sep}}$. During the transition, the electric-field well deepens, suppressing turbulent transport and steepening the edge pressure profile (Figs. 1 and 2). Conversely, for the same input power, the unfavourable simulation shows neither improved confinement nor significant changes in the electric field. Repeating the ramp at roughly twice the L-mode input power, the unfavourable case also transitions to a high confinement mode, with a similar deepening of the electric-field

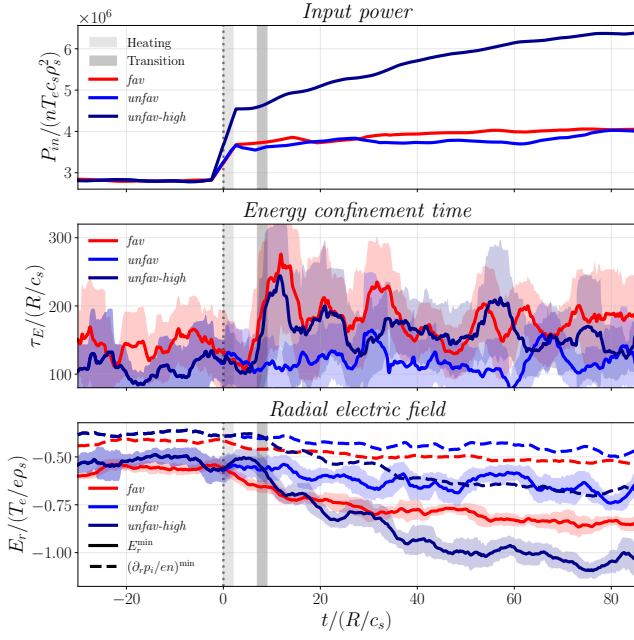


FIG. 1: Time traces of injected power P_{in} (top), energy confinement time τ_E (middle), minima of radial electric field E_r^{min} and ion pressure gradient $(\partial_r p_i/en)^{min}$ (bottom), for simulations in the favourable magnetic field direction (*fav*, red), unfavourable (*unfav*, blue) and unfavourable at higher power (*unfav-high*, dark-blue).

well as in the favourable case. Edge turbulence prior to the transition arises from a combination of resistive ballooning and electron drift-wave (DW) modes. Removing the curvature drive from the simulations substantially suppresses turbulence, confirming the role of interchange modes, and spatio-temporal Fourier analysis reveals DW signatures: $\omega \simeq \omega_*$ and $e\phi/\langle T_e \rangle \sim \tilde{n}/\langle n \rangle \sim \tilde{p}_e/\langle p_e \rangle$ (fluctuations are denoted by $\tilde{f} = f - \langle f \rangle$, with $\langle f \rangle$ the time- and flux-surface average).

Simulations show that a transport barrier only forms when the edge plasma- β exceeds a critical value, consistent with previous flux-tube results [5]. Two electromagnetic mechanisms drive the suppression: linear DW stabilisation via enhanced electron adiabatic response [21, 22], and nonlinear $\mathbf{E} \times \mathbf{B}$ shear generation by finite- β DWs [6]. In fact, artificially removing the zonal component of the $\mathbf{E} \times \mathbf{B}$ drift from the simulations immediately restores high transport levels, confirming its role in barrier formation. The rise of $\mathbf{E} \times \mathbf{B}$ shear observed in the simulations originates from turbulent generation of momentum flux, as revealed by analysing the radial electric field evolution equation. Indeed, in the drift-reduced Braginskii model implemented in GBS, the flux-surface-averaged radial electric field evolves according to $\partial_t \langle \mathcal{E}_r \rangle = \mathcal{F}$, where $\mathcal{E}_r = -(dr/d\psi) nm_i |\nabla \psi|^2 E_r / B^2$ and $\mathcal{F} = \langle J_{\parallel} \delta \mathbf{B} \cdot \nabla \psi / B \rangle - \langle \mathbf{v}_E \cdot \nabla \varpi \cdot \nabla \psi \rangle$ encodes the nonlinear momentum flux (Maxwell and Reynolds stress).

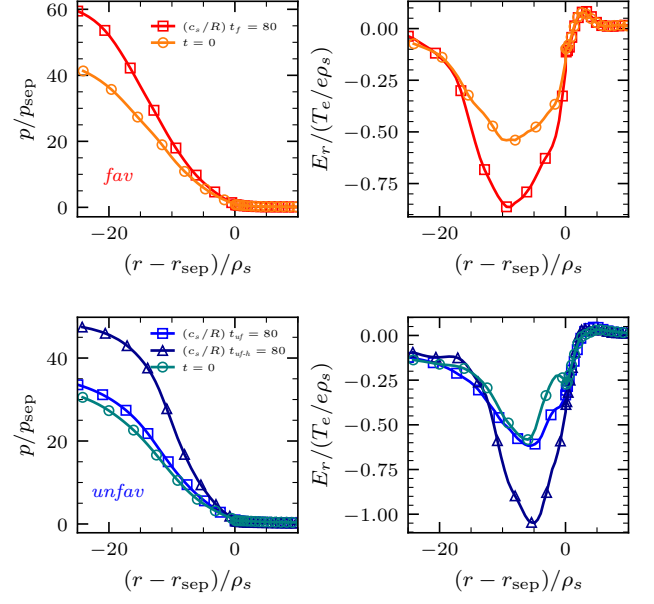


FIG. 2: Radial profiles of flux-surface-averaged total pressure p (normalised to the separatrix value p_{sep}) and radial electric field E_r , at $t=0$ and at $t=80 R/c_s$. Favourable (top) and unfavourable (bottom), with the latter shown at both matched input power (blue squares), and higher power (dark-blue triangles).

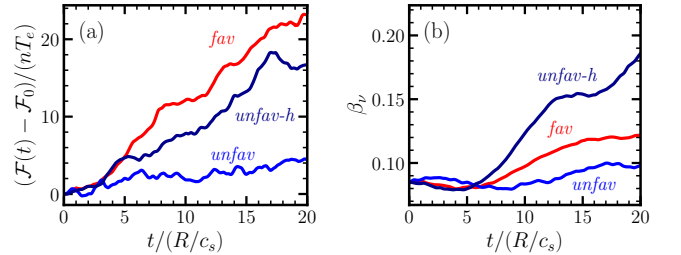


FIG. 3: (a) Turbulent momentum flux $\mathcal{F}(t) - \mathcal{F}_0$ following the onset of additional heating, with $\mathcal{F}_0 \equiv \mathcal{F}(t=0)$ subtracted to highlight the transition dynamics. (b) Time trace of β_{ν} at the radial electric-field minimum position.

Here, $\varpi = (nm_i/B^2)(\nabla_{\perp} \phi + \nabla_{\perp} p_i/en)$ is the generalised vorticity, $\delta \mathbf{B} = \nabla \times (A_{\parallel} \mathbf{b})$ the perturbed magnetic field, and \mathbf{v}_E the $\mathbf{E} \times \mathbf{B}$ drift velocity. Gyro-viscosity, parallel vorticity advection, radial diamagnetic current flux, and $\partial_t (\partial_r p_i/en)$ are neglected in the expression for \mathcal{F} , yielding small contributions to $\partial_t E_r$. Figure 3a shows the nonlinear momentum flux \mathcal{F} at the position of the electric-field-well minimum, $r = r_{min}$, as a function of time during the transition phase, $t \in (0, 20R/c_s)$. The unfavourable configuration shows no change in the nonlinear drive of mean $\mathbf{E} \times \mathbf{B}$ flow unless a higher input power is used, an observation that recalls the asymmetry effect recently

identified in L-mode simulations of AUG [23]. Since confinement transitions occur only if accompanied by strong growth of mean $\mathbf{E} \times \mathbf{B}$ flow (Fig. 3), consistent with experiments and previous simulations [15, 17, 24, 25], we derive the conditions under which finite- β DWs can drive the formation of a mean flow, showing that the threshold criterion is more easily accessed in the favourable configuration.

Adopting a local straight-field-line coordinate system, centred at the $\psi = \psi_0$ flux-surface and given by $x = |q_0|(\psi - \psi_0)/(r_0 B)$, $y = \sigma_T \sigma_p r_0 (q\theta - \varphi)/|q_0| + \sigma_T \hat{s} \Omega_E x t$ and $z = qR\theta$, the magnetic field is expressed as $\mathbf{B} = \sigma_T B \nabla x \times \nabla y$ [26, 27]. The coordinate θ is the straight-field-line angle, with $\theta = 0$ at the outer-midplane. The $\mathbf{E} \times \mathbf{B}$ shearing rate normalised to magnetic shear is given by $\Omega_E = -(\rho_s c_s |q| R / v_A) d_x^2 \langle \phi \rangle / \hat{s}$, where $L_n = 1/|d_x \log \langle n \rangle|$ and $v_A = B / \sqrt{\mu_0 m_i \langle n \rangle}$ is the Alfvén velocity. Starting from the drift-reduced Braginskii model, assuming cold ions, weak curvature, and neglecting coupling to sound-waves ($k_{\parallel} c_s \ll \partial_t \sim \omega_* = k_y \rho_s c_s / L_n$), we derive the DW system, yielding

$$\frac{\partial n}{\partial t} + i \sigma_T \rho_s k_y \sqrt{\beta_A} \phi + \sigma_p \frac{\partial(\rho_s^2 k_{\perp}^2 A_{\parallel})}{\partial \theta} = 0, \quad (2)$$

$$\frac{\partial(\rho_s^2 k_{\perp}^2 \phi)}{\partial t} - \sigma_p \frac{\partial(\rho_s^2 k_{\perp}^2 A_{\parallel})}{\partial \theta} = 0, \quad (3)$$

$$\begin{aligned} \frac{\partial}{\partial t} \left(1 + \frac{\rho_s^2 k_{\perp}^2}{\beta_{\mu}} \right) A_{\parallel} + i \sigma_T \rho_s k_y \sqrt{\beta_A} A_{\parallel} \\ - \sigma_p \frac{\partial(\phi - n)}{\partial \theta} + \frac{\rho_s^2 k_{\perp}^2}{\beta_{\nu}} A_{\parallel} = 0, \end{aligned} \quad (4)$$

where the perpendicular wavenumber,

$$k_{\perp}^2 = k_y^2 \left[\frac{1}{g} + \hat{s}^2 (\theta + r_0 \partial_x \theta / \hat{s} - \sigma_T \Omega_E t)^2 g \right], \quad (5)$$

acquires its characteristic time-dependence in a radially-varying background flow [26, 27], with modes sheared along the field-lines by \hat{s} , and in time by $\mathbf{E} \times \mathbf{B}$ shear. We denote the radial metric element as $|\nabla x|^2 \equiv g(\theta, r_0)$. In Eqs. (2–4), the fields are normalised as $e\phi/\langle T_e \rangle \rightarrow \phi$, $[\Omega_i v_A / (c_s^2 B)] A_{\parallel} \rightarrow A_{\parallel}$, $n/\langle n \rangle \rightarrow n$, and time is normalised to the Alfvén frequency, $\omega_A = v_A / (|q|R)$. Three main parameters regulate the model in Eqs. (2–4): $\beta_{\nu} = \beta \omega_A / (2\nu)$, related to finite collisionality driving resistive DWs (RDWs), $\beta_{\mu} = \beta / (2\mu)$, associated with finite electron mass $m_e = \mu m_i$ driving inertial DWs (IDWs), and $\beta_A = (\omega_* / \omega_A)^2 / (k_y \rho_s)^2$, being the ratio between the electron diamagnetic and the Alfvén frequencies. Linearly, DWs are strongly suppressed by electromagnetic effects with increasing β_{ν} (RDW branch) or β_{μ} (IDW branch) [22]. The parameter β_A instead describes the coupling between Alfvén waves and DWs, which becomes important for $\beta_A \sim 1$ [28]. Balancing the inertial and resistive terms in Eq. (4) [29], one finds that resistive effects dominate over inertial effects when

$\beta_{\nu} / \beta_{\mu} = \mu \omega_A / \nu \equiv \hat{\mu} \ll 1$, the regime of the GBS simulations presented here. Within the approximations used to derive Eqs. (2–4), the evolution equation of the electric field, $\partial_t \langle \mathcal{E}_r \rangle = \mathcal{F}$, becomes

$$\frac{\rho_s}{\sqrt{\beta_A} L_n} \frac{\partial}{\partial t} \frac{d \langle \phi \rangle}{dx} + \sigma_T \frac{d \Pi}{dx} = 0, \quad (6)$$

where the turbulent stress, $\Pi = \sum_{k_y} \Pi_{k_y}$, is expressed as

$$\Pi_{k_y} = \rho_s^2 k_y^2 \left\langle \frac{g}{\langle g \rangle} \hat{s} (\theta - \sigma_T \Omega_E t) (|\phi|^2 - |A_{\parallel}|^2) \right\rangle, \quad (7)$$

and is computed quasilinearly, by using the solutions for ϕ and A_{\parallel} obtained from the linear problem, Eqs. (2–4). In the chosen coordinates, $\langle f \rangle = \int_{-\tau/2}^{\tau/2} dt \int_{-\infty}^{\infty} d\theta f(\theta, t) / (\tau L_{\theta})$, where $L_{\theta} = \int_{|f|>0} d\theta$ and $\tau > 0$ is a time-integration interval, chosen to be the turbulence decorrelation time, $\tau = 1/|\Omega_E|$ [30]. The net momentum flux across the pedestal region $r \in (r_-, r_+)$ around the electric field minimum r_{\min} ($r_{\pm} = r_{\min} \pm 2\rho_s$) is obtained by integrating Eq. (6), yielding $-\sigma_T [\Pi(r_+) - \Pi(r_-)]$. Mean flow growth, $\partial_t [\langle \phi \rangle(r_+) - \langle \phi \rangle(r_-)] > 0$, therefore requires $-\sigma_T [\Pi(r_+) - \Pi(r_-)] > 0$. In the RDW regime ($\mu \propto 1/\beta_{\mu} = 0$), this condition is met once β_{ν} exceeds a critical value $\beta_{\nu}^*(\sigma_T)$, shown in the left panel of Fig. 4. The resulting rise in $\mathbf{E} \times \mathbf{B}$ shear acts to increase β_{ν} by suppressing turbulence, further increasing $\mathbf{E} \times \mathbf{B}$ shear. The edge thus becomes unstable to the spontaneous formation of a pedestal, accessing a regime of suppressed transport and large electric field shear. Both $\beta_{\nu}^*(\sigma_T = -1) \simeq 0.07$ and the asymmetry ratio $\beta_{\nu}^*(\sigma_T = 1) / \beta_{\nu}^*(\sigma_T = -1) \sim 2$ (middle panel of Fig. 4) are slow-varying functions of β_A and Ω_E over an experimentally relevant range. These estimates agree well with the simulation results in Fig. 3b, in which β_{ν} is shown at $r = r_{\min}$ as a function of time. The favourable configuration transitions to a suppressed transport regime for $\beta_{\nu} \simeq 0.09$ (at $t \simeq 10$), while the unfavourable configuration at matched power does not, transitioning instead at higher power, once $\beta_{\nu} \simeq 0.13$. In the inertial limit $\nu \propto 1/\beta_{\nu} = 0$, where IDWs dominate, a transition to a suppressed transport regime occurs once $\beta_{\mu} > \beta_{\mu}^*$, the threshold value shown in the right panel of Fig. 4.

We now discuss the symmetry properties of Eqs. (2–6). The transformation $\sigma_p \rightarrow -\sigma_p, A_{\parallel} \rightarrow -A_{\parallel}$ leaves the system invariant, implying that $\Pi^{\sigma_p} = \Pi^{-\sigma_p}$. This is in agreement with the experimental observation that reversing the direction of the plasma current does not influence the L–H power threshold [13]. Indeed, we verify that reversing the sign of σ_p does not affect the GBS simulation results. Meanwhile, the field-reversal symmetry $\sigma_T \rightarrow -\sigma_T$ is broken only when four conditions hold simultaneously: (i) finite collisionality ($\nu \neq 0$), which breaks the time-reversal invariance ($\sigma_T, \sigma_p, t \rightarrow (-\sigma_T, -\sigma_p, -t)$); (ii) finite $\mathbf{E} \times \mathbf{B}$ shear ($\Omega_E \neq 0$) and

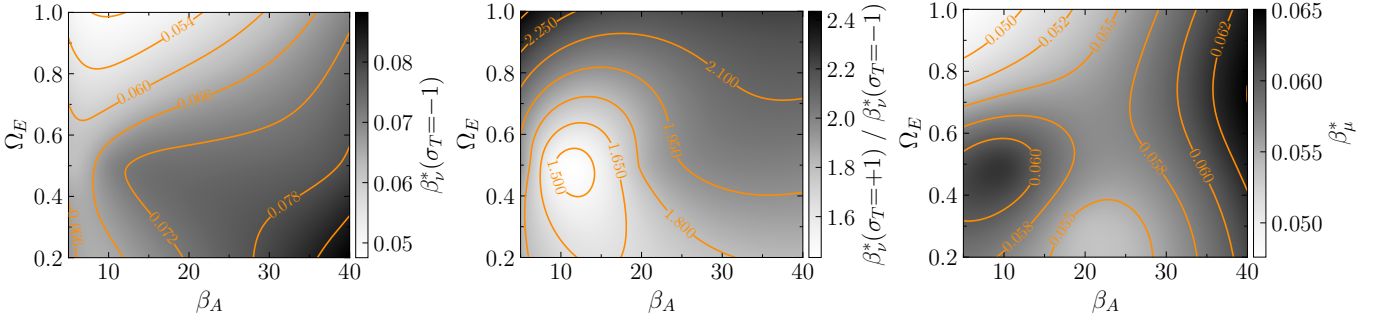


FIG. 4: Mean flow generation critical parameter in the RDW regime: favourable configuration, $\beta_\nu^*(\sigma_T = -1)$ (left) and asymmetry ratio, $\beta_\nu^*(\sigma_T = +1)/\beta_\nu^*(\sigma_T = -1)$ (middle). Critical parameter in the IDW regime, β_μ^* (right).

(iii) finite magnetic shear ($\hat{s} \neq 0$), which together break the $(\sigma_T, k_y) \rightarrow (-\sigma_T, -k_y)$ symmetry; and (iv) up-down geometric asymmetry, $g(\theta) \neq g(-\theta)$, which breaks the $(\sigma_T, \sigma_p, \theta) \rightarrow (-\sigma_T, -\sigma_p, -\theta)$ symmetry mapping $\Pi \rightarrow -\Pi$.

Using the transition criteria derived from the quasilinear theory, $\beta_\nu > \beta_\nu^*(\sigma_T)$ and $\beta_\mu > \beta_\mu^*$, we now obtain first-principles scaling laws for the L–H power threshold in the high- and low-density branches, as well as the density minimum and its associated power. The power crossing the last-closed-flux-surface (LCFS) is given by $P = \int Q_\perp dS$, with Q_\perp the radial heat flux density, integrated over the surface $S = \int dS$. Using a mixing-length estimate for turbulent transport, we have $Q_\perp \sim \gamma|\partial_x p|/k_x^2 \sim \gamma p/k_y$, where we use the non-local linear scaling relation $k_x \sim \sqrt{k_y/L_p}$ [21, 31, 32], valid for both DW and ballooning instabilities. For the DW instability, $\gamma/k_y \sim \rho_s c_s/L_n$ [29], and balancing cross-field transport against conduction-limited parallel losses [8, 33], one obtains a relation between the power and the gradient length-scales, $L_n \sim L_p$, given by $P \sim nS [7qL_\parallel P/(4\pi aL_p\chi_0)]^{4/7}/(eBLn)$, where $\chi_0 = (4\pi\epsilon_0/e^2)^2/(\sqrt{m_e}Z_{\text{eff}}\Lambda)$ and Λ is the Coulomb logarithm. The transition parameters, β_ν and β_μ , can now be expressed solely as functions of engineering variables. Imposing $\beta_\nu \gtrsim \beta_\nu^*(\sigma_T)$ (RDW), and $\beta_\mu \gtrsim \beta_\mu^*$ (IDW), and estimating $S \simeq 4\pi^2 aR$ and $L_\parallel \simeq 2\pi qR$, we obtain expressions for the threshold power in the high-density branch,

$$P_\nu = K_\nu \frac{\beta_\nu^*(\sigma_T)^{11/10} e^{19/10} \Lambda^{3/5} m_e^{3/10}}{\mu_0^{11/20} \epsilon_0^{6/5} m_h^{11/20}} \times \frac{aR^{11/10} B^{3/5} n^{21/20} Z_{\text{eff}}^{3/5} q^{1/10}}{M^{11/20}}, \quad (8)$$

and in the low-density branch,

$$P_\mu = K_\mu \frac{\beta_\mu^{*11/4} \epsilon_0 m_e^{5/2}}{e^{5/2} \sqrt{\Lambda} \mu_0^{11/4} m_h^{11/4}} \frac{aB^5}{n^{9/4} q \sqrt{Z_{\text{eff}} M^{11/4}}}, \quad (9)$$

respectively. We denote the main ion mass number by

$M = m_i/m_h$, with m_h the hydrogen mass, and we introduce the dimensionless factors K_ν and K_μ to account for $O(1)$ scaling approximations in the derivation (the only free parameters in Eqs. (8) and (9)). In Fig. 5b, we compare the analytical scaling law in the high-density branch, Eq. (8), against the ITPA experimental database for high-density transitions in the favourable configuration [14]. Estimating the threshold parameter via the quasilinear result in Fig. 4, $\beta_\nu^*(\sigma_T = -1) = 0.07$, and choosing the fitting constant in Eq. (8) to be $K_\nu = 0.325$, we obtain $R^2 = 0.87$. The empirical scaling law, Eq. (1), achieves instead $R^2 = 0.83$ (Fig. 5a). We note that the theoretical scaling law in Eq. (8), $P_\nu \sim aR^{11/10} B^{3/5} n^{21/20}$, also agrees with the recently revised ITPA scaling law for metal-wall devices (ITER-like wall), found to scale as $P_{\text{ILW}}^{\text{ITPA}} \sim aR B^{0.58} n^{1.08}$ [36]. Moreover, the effective charge scaling exponent $Z_{\text{eff}}^{3/5}$ in Eq. (8) agrees with the experimentally observed dependence $\sim Z_{\text{eff}}^{0.7}$ [13, 37]. Combining Eq. (8) with the quasilinear results shown in Fig. 4, the power asymmetry factor is approximately $P_\nu(\sigma_T = +1)/P_\nu(\sigma_T = -1) = [\beta_\nu^*(\sigma_T = +1)/\beta_\nu^*(\sigma_T = -1)]^{11/10} \sim 2$, consistent with experimental observations [13]. A comparison of the analytical high- and low-density branch scaling laws, Eqs. (8) and (9), with TCV data, is shown in Fig. 5d, revealing good agreement. In the sheath-limited regime [33], the low-density branch scaling is modified to $P'_\mu = K'_\mu (m_e^{7/4}/\sqrt{e} m_h^2 \mu_0^{7/4}) aB^3 R^{1/2} n^{-3/4} Z^{1/4} M^{-2}$, with a weaker density dependence than Eq. (9), consistent with AUG and JET observations [35, 38]. In AUG, for $P \gtrsim 1$ MW, sheath-limited conditions are expected to occur at separatrix densities $n_{\text{sep}} \lesssim 10^{19} \text{ m}^{-3}$, typically achieved in low-density AUG scenarios [39]. The scaling for P'_μ indeed describes AUG data [35] across three values of I_p remarkably well (Fig. 5d).

We propose that the crossover point between the low- and high-density branches of the L–H transition occurs when inertial and resistive effects are comparable, $\hat{\mu} \sim 1$.

This yields a scaling law for the density minimum n_{\min} ,

$$n_{\min} = K_n \frac{\epsilon_0^{2/3} m_e^{2/3}}{e^{4/3} \mu_0^{1/3} \Lambda^{1/3} m_h^{2/3}} \frac{I_p^{1/3} B}{Z_{\text{eff}}^{1/3} a^{2/3} M^{2/3}}, \quad (10)$$

where the power P is evaluated with the high-density scaling law, Eq. (8). Substituting Eq. (10) in Eq. (8), one finds an expression for the minimum power required to access an H-mode regime,

$$P_{\min} = K_P \frac{e^{1/2} \Lambda^{1/4} m_e a^{1/2} R B^{7/4} I_p^{1/4} Z_{\text{eff}}^{1/4}}{\epsilon_0^{1/2} m_h^{5/4} \mu_0 M^{5/4}}, \quad (11)$$

where the safety factor is expressed in terms of the plasma current I_p , via $q \sim 2\pi a^2 B / (\mu_0 R I_p)$. Eqs. (10) and (11) are in good agreement with existing empirical

scalings [9] and, choosing $K_n = 1.21$ (fitted to data) and $K_P = K_n \beta_\nu^* (\sigma_T = -1)^{11/10} K_n^{21/20} = 0.0213$ (not fitted), describe very well the experimental data in Table 1 of [36] for ITER-like wall devices (Figs. 5e and 5f). In TCV, the measured P_{\min} and n_{\min} exceed the predicted values (Fig. 5c), plausibly due to unsubtracted radiative losses and, for the latter, to the dominant use of electron-cyclotron heating at low densities in [34], which lowers edge collisionality and shifts the $\hat{\mu} \sim 1$ crossover to higher density. Finally, though we find that the isotope scaling of the threshold power, $P_\nu \sim M^{-11/20}$ in Eq. (8), is weaker than the experimentally observed trend, $P_{\text{LH}} \sim 1/M$ [36], the minimum threshold power $P_{\min} \sim M^{-5/4}$ in Eq. (11) closely matches the empirical exponent.

Turning now to ITER's full-field scenario ($I_p = 15$ MA, $B = 5.3$ T), setting $Z_{\text{eff}} = 1.5$ and $M = 2.5$ (DT mixture), Eqs. (10) and (11) yield $n_{\min} = (5.8 \pm 1.0) \times 10^{19} \text{m}^{-3}$ and $P_{\min} = (43 \pm 11)$ MW, with uncertainties estimated from the root-mean-square error (RMSE) values. We therefore expect ITER to achieve H-mode within its planned auxiliary heating limit of 73 MW [40]. In the full-field scenario of SPARC ($I_p = 8.7$ MA, $B = 12.2$ T) [3], we find, instead, $n_{\min} = (2.6 \pm 0.4) \times 10^{20} \text{m}^{-3}$ and $P_{\min} = (26 \pm 7)$ MW, leaving little margin relative to the planned 25 MW heating capacity, a concern already raised in [41] and derived here from first principles.

Acknowledgments. We thank F. Ryter for providing access to AUG data and for his insightful comments, as well as L. Aucone, J. Ball, S. Brunner, B. Frei, M. Giacomini, T. Görler, Y. Martin, M. Pedrini, E. Tonello, and the TSVV-A group for helpful discussions. The simulations in this work were run on Daint (s1170), Daint-ALPS (lp129) and Discoverer (EHPC-REG-2023-R01-138). This work has been carried out within the framework of the EUROfusion Consortium, partially funded by the European Union via the Euratom Research and Training Programme (Grant Agreement No 101052200 — EUROfusion). The Swiss contribution to this work has been funded in part by the Swiss State Secretariat for Education, Research and Innovation (SERI). Views and opinions expressed are however those of the author(s) only and do not necessarily reflect those of the European Union, the European Commission or SERI. Neither the European Union nor the European Commission nor SERI can be held responsible for them. This work was supported in part by the Swiss National Science Foundation.

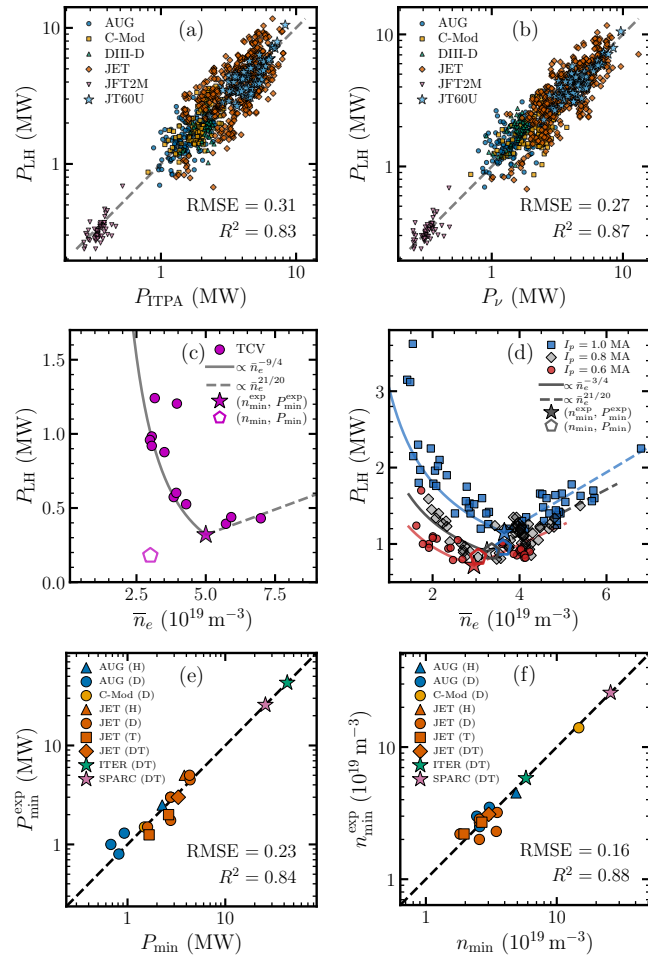


FIG. 5: Favourable configuration L–H power threshold: empirical (a) from Eq. (1), and analytical (b), from Eq. (8) (using $\Lambda = 15$ and, when missing, $Z_{\text{eff}} = 1.5$). Low- and high-density branches in TCV (c) and AUG (d) (data from [34] and [35]). P_{LH} minimum (e) and density minimum (f), with data from [36], and predictions for ITER and SPARC.

* brenno.delucca@epfl.ch

- [1] F. Wagner *et al.*, Phys. Rev. Lett. **49**, 1408 (1982).
- [2] E. Doyle *et al.*, Nuclear Fusion **47**, S18 (2007).
- [3] A. J. Creely *et al.*, Journal of Plasma Physics **86**,

- 865860502 (2020).
- [4] O. P. Pogutse *et al.*, in *Proceedings of the 24th European Conference on Controlled Fusion and Plasma Physics* (Berchtesgaden, 1997) p. 1041.
- [5] B. N. Rogers, J. F. Drake, and A. Zeiler, *Phys. Rev. Lett.* **81**, 4396 (1998).
- [6] P. N. Guzdar *et al.*, *Phys. Rev. Lett.* **87**, 015001 (2001).
- [7] E. Kim and P. H. Diamond, *Phys. Rev. Lett.* **90**, 185006 (2003).
- [8] W. Fundamenski *et al.*, *Nucl. Fusion* **52**, 062003 (2012).
- [9] F. Ryter *et al.*, *Nuclear Fusion* **54**, 083003 (2014).
- [10] T. Eich, P. Manz, and the ASDEX Upgrade team, *Nucl. Fusion* **61**, 086017 (2021).
- [11] S. J. Fielding *et al.*, *Plasma Physics and Controlled Fusion* **38**, 1091 (1996).
- [12] ASDEX Team, *Nucl. Fusion* **29**, 1959 (1989).
- [13] T. Takizuka and ITPA H-mode Power Threshold Database Working Group, *Plasma Phys. Control. Fusion* **46**, A227 (2004).
- [14] Y. R. Martin, T. Takizuka, and ITPA CDBM H-mode Threshold Database Working Group, *J. Phys.: Conf. Ser.* **123**, 012033 (2008).
- [15] C. S. Chang *et al.*, *Phys. Rev. Lett.* **118**, 175001 (2017).
- [16] M. Giacomini and P. Ricci, *Journal of Plasma Physics* **86**, 905860502 (2020).
- [17] W. Zholobenko *et al.*, *Phys. Rev. Lett.* **136**, 075101 (2026).
- [18] P. Ricci *et al.*, *Plasma Phys. Control. Fusion* **54**, 124047 (2012).
- [19] M. Giacomini *et al.*, *J. Comput. Phys.* **463**, 111294 (2022).
- [20] B. Duval *et al.*, *Nuclear Fusion* **64**, 112023 (2024).
- [21] B. N. Rogers and W. Dorland, *Phys. Plasmas* **12**, 062511 (2005).
- [22] A. Masetto *et al.*, *Phys. Plasmas* **19**, 112103 (2012).
- [23] B. J. Frei *et al.*, *Phys. Rev. Lett.* (2025), submitted.
- [24] R. J. Groebner, K. H. Burrell, and R. P. Seraydarian, *Phys. Rev. Lett.* **64**, 3015 (1990).
- [25] I. Cziegler *et al.*, *Phys. Rev. Lett.* **118**, 105003 (2017).
- [26] F. L. Waelbroeck and L. Chen, *Phys. Fluids B* **3**, 601 (1991).
- [27] S. L. Newton, S. C. Cowley, and N. F. Loureiro, *Plasma Phys. Control. Fusion* **52**, 125001 (2010).
- [28] P. N. Guzdar *et al.*, *Physics of Plasmas* **8**, 3907 (2001).
- [29] P. Ricci and B. N. Rogers, *Phys. Rev. Lett.* **104**, 145001 (2010).
- [30] H. Biglari, P. H. Diamond, and P. W. Terry, *Phys. Fluids B* **2**, 1 (1990).
- [31] P. Ricci and B. N. Rogers, *Phys. Plasmas* **16**, 062303 (2009).
- [32] Z. Tecchiolli *et al.*, *Physics of Plasmas* **32**, 102303 (2025).
- [33] P. C. Stangeby, *The Plasma Boundary of Magnetic Fusion Devices*, 1st ed. (CRC Press, 2000).
- [34] F. Piras *et al.* (TCV Team), *Phys. Rev. Lett.* **105**, 155003 (2010).
- [35] F. Ryter *et al.*, *Nucl. Fusion* **53**, 113003 (2013).
- [36] E. Delabie *et al.*, *Nuclear Fusion* **66**, 036016 (2026).
- [37] G. Birkenmeier *et al.*, *Nuclear Fusion* **66**, 026024 (2026).
- [38] C. F. Maggi *et al.*, *Nucl. Fusion* **54**, 023007 (2014).
- [39] M. Cavedon *et al.*, *Nuclear Fusion* **65**, 106007 (2025).
- [40] A. Loarte *et al.*, *Plasma Phys. Control. Fusion* **67**, 065023 (2025).
- [41] J. Hughes *et al.*, *Nuclear Fusion* **65**, 052001 (2025).